Microsc. Microanal. 19, 716–725, 2013
doi:10.1017/S1431927613000342

Microscopy AND Microanalysis

Selenium Segregation in Femtosecond-Laser Hyperdoped Silicon Revealed by Electron Tomography

Georg Haberfehlner,[1,*] Matthew J. Smith,[2] Juan-Carlos Idrobo,[3] Geoffroy Auvert,[4] Meng-Ju Sher,[5] Mark T. Winkler,[5] Eric Mazur,[5] Narciso Gambacorti,[1] Silvija Gradečak,[2] and Pierre Bleuet[1]

[1]*CEA, LETI, MINATEC Campus, 17 rue des Martyrs, 38054 Grenoble Cedex 9, France*
[2]*Department of Materials Science and Engineering, Massachusetts Institute of Technology, Cambridge, MA 02139, USA*
[3]*Materials Science and Technology Division, Oak Ridge National Laboratory, Oak Ridge, TN 37831, USA*
[4]*STMicroelectronics, 850 Rue Jean Monnet, 38926 Crolles, France*
[5]*Department of Physics and School of Engineering and Applied Sciences, Harvard University, Cambridge, MA 02138, USA*

Abstract: Doping of silicon with chalcogens (S, Se, Te) by femtosecond laser irradiation to concentrations well above the solubility limit leads to near-unity optical absorptance in the visible and infrared (IR) range and is a promising route toward silicon-based IR optoelectronics. However, open questions remain about the nature of the IR absorptance and in particular about the impact of the dopant distribution and possible role of dopant diffusion. Here we use electron tomography using a high-angle annular dark-field (HAADF) detector in a scanning transmission electron microscope (STEM) to extract information about the three-dimensional distribution of selenium dopants in silicon and correlate these findings with the optical properties of selenium-doped silicon. We quantify the tomography results to extract information about the size distribution and density of selenium precipitates. Our results show correlation between nanoscale distribution of dopants and the observed sub-band gap optical absorptance and demonstrate the feasibility of HAADF-STEM tomography for the investigation of dopant distribution in highly-doped semiconductors.

Key words: electron tomography, HAADF-STEM, femtosecond pulsed laser irradiation, optical hyperdoping, dopant segregation

Introduction

Enabling silicon to absorb in the infrared range is of great interest for silicon-based infrared optoelectronic devices (Carey et al., 2005). One route toward tailoring of the optoelectronic properties of silicon is doping with chalcogens (S, Se, Te) to concentrations well above the solubility limit. This process, known as optical hyperdoping, can produce broad-band absorption in the infrared (IR) range. Optical hyperdoping can be obtained by the irradiation of silicon with femtosecond (fs) laser pulses in the presence of a dopant precursor, either a gas-phase precursor such as sulfur hexafluoride (SF_6) (Wu et al., 2001; Younkin et al., 2003) or a thin film precursor (Sheehy et al., 2007; Tull et al., 2009; Smith et al., 2011*a*). When doping is done with conventional methods—for example, vapor diffusion or ion implantation (followed by annealing)—the dopant concentration is limited by their equilibrium solid solubility limit to 10^{16}–10^{17} cm^{-3} (Vydyanath et al., 1978), while optical hyperdoping can yield concentrations in the range of 10^{19}–10^{20} cm^{-3} (Sher et al., 2011).

It has been shown that the supersaturated concentrations of chalcogens give rise to strong sub-band gap absorptance in silicon (Sheehy et al., 2007), but the nature of the IR absorptance is still poorly understood. A useful approach to understanding how the dopant distribution influences the absorptance is through monitoring the decay in sub-band gap absorptance with annealing (Tull et al., 2009). It has been shown that the reduction of sub-band gap absorptance scales with both annealing time and temperature in a way that is proportional to the diffusion length of the dopant at a given annealing condition. The evolution of the chemical state of selenium with annealing has also been investigated by extended X-ray absorptance fine structure (EXAFS) spectroscopy and showed a shift in the chemical state of selenium with annealing that is closely related to the observed decay in sub-band gap absorptance (Newman et al., 2009). Despite the improved understanding of the diffusion-limited kinetics and changes in chemical state that occur during the annealing of selenium-hyperdoped silicon, no direct structural evidence of dopant diffusion or phase segregation has been observed.

Electron tomography based on scanning transmission electron microscopy (STEM) using a high-angle annular dark-field (HAADF) detector is an efficient method to distinguish between materials with differences in their atomic number and provides nanometer resolution in three dimensions (Midgley & Weyland, 2003; Midgley & Dunin-Borkowski, 2009). The sensitivity of HAADF-STEM to the atomic number allows for the detection of heavy atoms in a lighter environment and is thereby well suited for studying the distribution of dopants with sufficient mass contrast. Segregation has been studied using electron tomography at a larger scale for the identification of germanium precipitates in an Al-Ge alloy using HAADF-STEM (Kaneko et al., 2008) and for the studies of oxide precipitates in silicon

Received October 19, 2012; accepted January 30, 2013
*Corresponding author. E-mail: georg.haberfehlner@cea.fr

using bright-field transmission electron microscopy (TEM) tomography (Schierning et al., 2011). Another frequently used method for studies of dopant segregation is atom probe tomography (Thompson et al., 2005; Duguay et al., 2010; Jin et al., 2012), but atom probe tomography is not suited for the present case due to the strong structural disorder caused by the doping process, which makes evaporation of the material difficult. For very small samples electron tomography has been shown to provide near-atomic resolution (Scott et al., 2012) and even atomic resolution in combination with prior assumptions about the object (Bals et al., 2010; Van Aert et al., 2011; Goris et al., 2012*a*). For larger samples measuring few 100 nm, the achievable resolution is in the nanometer range.

In this work we investigate the distribution of selenium in fs-laser doped silicon before and after annealing using HAADF-STEM structural characterization. Cross-sectional investigations show inhomogeneous dopant distribution arising during fs-laser doping and provide initial observations of selenium segregation with annealing. Next, electron tomography is used to measure the three-dimensional (3D) distribution of selenium before and after annealing. A segmentation process is developed for quantifying the density and size distribution of precipitates, which takes into account the inhomogeneous dopant distribution in the starting material. Comparing these segmented reconstructions allows for confirmation of a large increase in the density of small (radius < 10 nm) precipitates and a decrease in the amount of selenium remaining in silicon as a solute.

Materials and Methods

Material Synthesis and Optical Characterization

To prepare selenium-hyperdoped silicon samples for this investigation, first a 75 nm film of selenium was deposited on boron-doped Si (100) wafers (resistivity $\rho = 1$–$20\ \Omega$ cm). Then, the wafers were irradiated with a 1 kHz train of 80 fs, 800 nm laser pulses with a fluence of 4 kJ/m^2 using 88 pulses per area. Post-irradiation annealing was done in a forming gas (5% H_2) environment. In this work, we compare the dopant distribution before and after annealing for 30 min at 950°C. A more detailed description of the hyperdoping process has been published elsewhere (Tull et al., 2009). Figure 1a shows a scanning electron microscope (SEM) image of the sample after doping. In addition to the incorporation of dopants, fs-laser doping also modifies the surface, producing a rough surface covered by periodic micron-scale peaks (Tull et al., 2006).

Optical properties of the samples before and after annealing have been investigated by measuring the IR absorptance with a UV-VIS-NIR (ultraviolet–visible–near infrared) spectrophotometer equipped with an integrating sphere (Tull et al., 2009; Smith et al., 2011*b*). The diffuse and specular reflectance (R) and transmittance (T) were measured, in 1 nm increments, to determine the absorptance ($A = 1 - R - T$) at each wavelength. Figure 1b shows the measured absorptance for the investigated samples. The

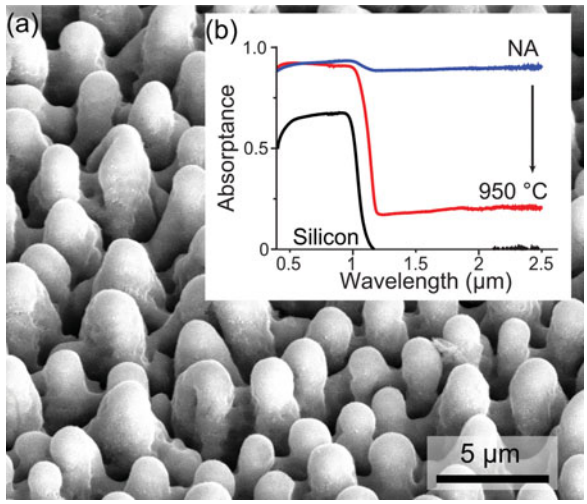

Figure 1. (**a**) SEM image of fs-laser doped silicon before annealing. The surface is covered by micron-scale peaks, which are formed during laser irradiation. (**b**) Absorptance of Se-hyperdoped silicon without any post-treatment annealing (blue, from Smith et al., 2011*a*) and after a 30 min anneal at 950°C (red), with the absorptance of an untreated silicon wafer for reference (black). Post-treatment annealing reduces the IR absorptance.

modified sample morphology influences the optical properties of silicon, increasing the absorptance due to enhanced geometrical light trapping (Sher et al., 2011). More importantly, the nonannealed sample shows near-unity absorptance for the whole investigated spectral range, extending well below the band gap, while for the 950°C annealed sample the sub-band gap absorptance is reduced to below 0.25. This annealing condition represents the extreme case; lower annealing temperatures and shorter annealing times provide samples with intermediate absorptance (Tull et al., 2009).

Sample Preparation

Cross-sectional TEM samples were prepared using a South Bay Technology Model 590 tripod polisher (South Bay Technology, Inc., San Clemente, CA, USA) and diamond polishing films on a Struers Labopol-4 polishing wheel (Struers, Copenhagen, Denmark). Final thinning of cross-sectional samples was carried out with an Ar^+-ion mill at 5 kV in a Gatan Precision Ion Polishing System (Gatan, Inc., Pleasanton, CA, USA).

Sample preparation for electron tomography was done in a FEI Strata dual-beam focused ion beam (FIB)/SEM (FEI Company, Hillsboro, OR, USA). The instrument is equipped with an *in situ* gas injection system with sources for deposition of silicon dioxide and tungsten as well as with a micromanipulator for extraction of the sample. The principles of sample preparation are shown in Figure 2. The goal of the preparation was to prepare a needle-shaped sample from the center of one of the peaks of the material, with a diameter of about 150 nm and a height of few micrometers. This type of sample preparation is now commonly used in electron tomography (Kawase et al., 2007;

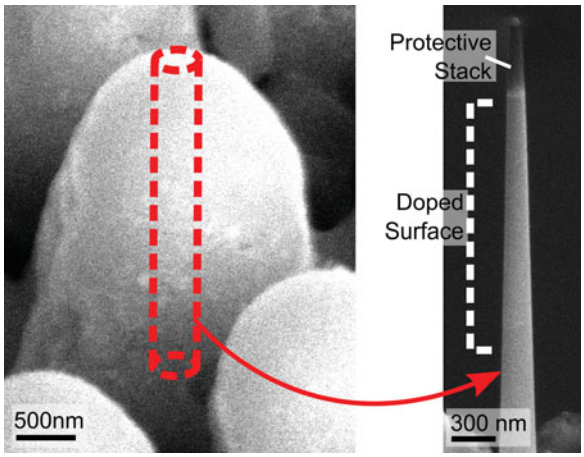

Figure 2. Principle of the sample preparation for electron tomography: needle-shaped samples are prepared from the center of peaks of the structured surface using a FIB/SEM instrument. The finished needle-shape samples contain a cylinder through the doped silicon surface.

Yaguchi et al., 2008; Ke et al., 2010) as needle-shaped samples maximize the tilt range for tomography while keeping the sample thickness along the electron beam path small for all tilt angles. Preparing a relatively long needle allows the extraction of information about changes in sample composition with depth.

A protective stack, consisting of electron-deposited silicon dioxide, electron-deposited tungsten, and finally ion-deposited tungsten, was deposited on one of the micron-scale peaks on the surface prior to milling. Then a standard lift-out technique is used to extract a lamella with a thickness of 1–2 μm containing the protected peak. The extracted lamella is glued to an Omniprobe® TEM support grid (Omniprobe, Inc., Dallas, TX, USA). In contrast to standard TEM preparation, where the sample is usually glued to the side of one of the supporting posts of the TEM grid, we glued the lamella to the top of a support to prevent shadowing from the support at high tilt angles and to allow milling to a circular shape. To obtain a needle-shaped sample, annular milling at 30 kV was used, where the diameter of the milling pattern is reduced in several steps until a sample with a diameter of about 100 nm at the top remains. We abstained from finishing with ion milling at lower high tension, as this would reduce the inclination of sidewalls, thereby leading to a much larger sample diameter at the base of the peak. Our sample preparation produced samples with an inclination of the sidewalls of approximately 1.3°, causing the sample diameter to increase by 45 nm every 1 μm along the depth.

Cross-Sectional TEM Investigations

Cross-sectional HAADF-STEM characterization was conducted in a probe aberration-corrected FEI Titan 80–300 s microscope operated at 300 kV. The HAADF-STEM image in Figure 3a provides insights into the selenium distribution in a Se-hyperdoped region prior to annealing. Although

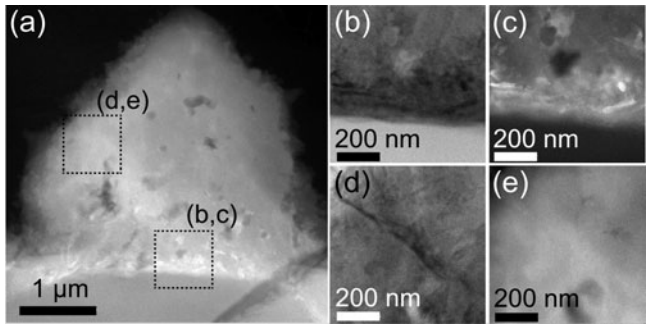

Figure 3. (**a**) HAADF-STEM image of a peak on the nonannealed surface of selenium-hyperdoped silicon. Brighter contrast within the peak is due to increased concentrations of selenium. (**b**) Bright-field STEM image of the interface between the polycrystalline hyperdoped region and the undoped silicon substrate, from region indicated in panel **a**. (**c**) HAADF-STEM image of the interface in panel **b**, showing diffuse contrast due to increased selenium concentrations, with some segregation already visible. (**d**) BF-STEM image of a grain boundary within the polycrystalline region. (**e**) HAADF-STEM image of the grain boundary in panel **d**, showing no visible signs of segregation. The dark spots visible in the HAADF-STEM image are voids.

HAADF-STEM does not directly give chemical information, comparing Figure 3a with previous investigations show that contrast changes observed in HAADF-STEM images correspond to changes in the selenium concentration in silicon (Sheehy et al., 2007; Smith et al., 2011*a*). Se-rich regions give brighter contrast due to the higher atomic number of selenium compared to silicon. The selenium concentrations are highest at the base of the peak, where the image contrast is diffuse and noticeably inhomogeneous (Figs. 3b, 3c). The contrast is also inhomogeneous throughout the body of the peak, though this may be exaggerated by changes in sample thickness. Close investigation of a grain boundary prior to annealing suggests no visible grain boundary segregation (Figs. 3d, 3e).

Annealing at 950°C for 30 min produces significant selenium segregation to grain boundaries and the precipitation of selenium-rich material, as shown in Figure 4a. At the base of the peak, where there was diffuse contrast before annealing, there is now a high density of selenium-rich precipitates, some of which exhibit faceting (Figs. 4b, 4c). A HAADF-STEM image of a grain boundary, from the region indicated in Figure 4a, shows selenium segregation into a region that is ~3 nm thick (Figs. 4d, 4e).

Comparing cross-sectional HAADF-STEM of the nonannealed selenium-hyperdoped silicon reveals an inhomogeneous selenium distribution within the surface peak. After annealing for 30 min at 950°C, we see evidence of selenium segregation with annealing. However, due to the complex 3D distribution of dopants, it is difficult to extract quantitative information about size and distribution of segregates from these cross-sectional images. To confirm and improve our understanding of selenium segregation with annealing, we therefore use HAADF-STEM tomography to map the selenium distribution in three dimensions.

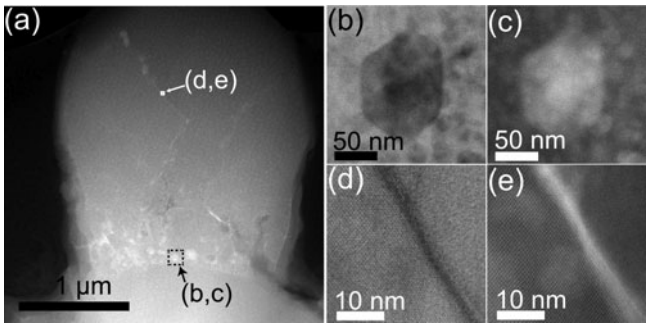

Figure 4. (**a**) HAADF-STEM image of a peak on the surface of selenium-hyperdoped silicon that was annealed for 30 min at 950°C. The base of the peak contains precipitates of selenium-rich material, and segregation to grain boundaries in the body of the peak is also visible. (**b**) Bright-field STEM image of a faceted Se-rich precipitate, from the region indicated in panel **a**. (**c**) HAADF-STEM image of the precipitate in panel **b**, confirming that it is selenium rich. (**d**) Bright-field STEM image of a grain boundary within the polycrystalline region. The region indicated in panel **a** is a best estimate of the image position. (**e**) HAADF-STEM image showing selenium segregation to grain boundary in panel **d**. Lighter contrast visible in panels **c** and **e** is ion beam damage due to sample preparation.

Electron Tomography Investigations

Electron tomography was performed on a probe aberration-corrected FEI 80-300 Titan microscope operated at 200 kV in HAADF-STEM mode. A small convergence angle of 5 mrad was used to improve the depth of field (Hyun et al., 2008). Projections of the needle-shaped samples were acquired over a tilt range of ±78° using a linear tilt step of 1°. The tilt range was limited by the used sample holder. Projections were acquired with a size of 2048 × 512 pixels at a pixel size of 1.03 nm. The voxel size of the reconstructed volumes is equal to the pixel size of the projections. Alignment of the tilt series was done by cross correlation using the FEI Inspect3D software. For the reconstruction a Matlab-based implementation of the simultaneous iterative reconstruction technique (Gilbert, 1972) with 20 iterations was used. For processing and visualization of the reconstructed volumes Matlab, ImageJ, and Avizo® were employed.

To enable the comparison of different reconstructions, we normalized the contrast in each reconstruction relative to two reference values; the mean value of the vacuum outside of the sample (set to 0) and the mean value of the undoped region in the bottom of the peaks (set to 1). The values of all voxels were normalized relative to those two values. Quantification of the selenium concentration would require both an exact knowledge of the Z-dependence of the contrast (Van Aert et al., 2009; Van den Broek et al., 2012) and detailed understanding of how selenium is incorporated in the silicon crystal structure. Therefore, in this investigation we concentrate on qualitative observations and, in particular, on the evolution in dopant distribution with annealing.

Figure 5 and Supplementary Movie 1 show volume-rendered views and slices through the reconstruction of the nonannealed sample. In agreement with the observations of the cross-sectional sample, the concentration of dopants is highest at the base of the peak. In the nonannealed sample, we observe diffuse contrast throughout the doped region, indicative of solid solution selenium incorporation and also some segregation of selenium-rich material. After a 30 min 950°C anneal (Fig. 6, Supplementary Movie 2), the dopant distribution is strongly inhomogeneous. We observe selenium segregation to grain boundaries as well as a large number of selenium-rich precipitates, in particular at the base of the peak, but also in the vicinity of the grain boundaries. Furthermore, the collection of this high-resolution structural information in three dimensions enables the quantification of dopant segregation with annealing.

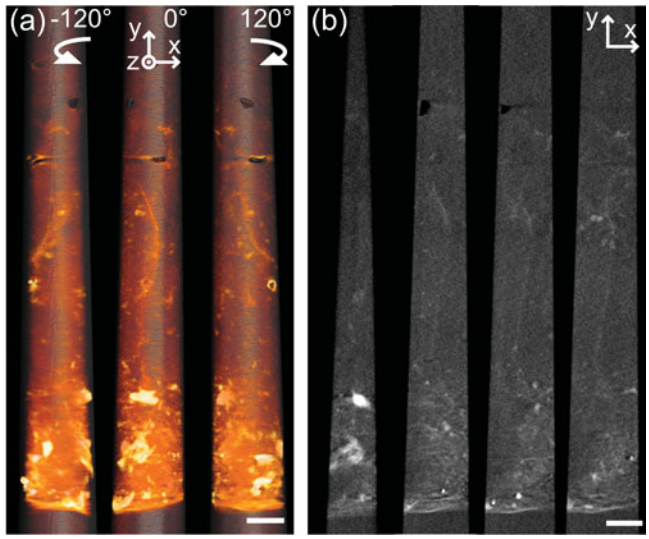

Figure 5. 3D reconstruction of the nonannealed sample: (**a**) Volume-rendered view from different viewing angles. Brighter regions correspond to higher selenium concentration. (**b**) Slices through the reconstructed volume at different locations along the z-direction. Diffuse contrast is visible at the base of the sample with some Se-rich precipitates. The selenium concentration increases toward the base of the sample. Scale bars = 100 nm. An animation showing all slices can be found as Supplementary Movie 1.

Supplementary Material

To view supplementary material for this article (including Supplementary Figs. 1–3, Supplementary Table 1, Supplementary Movies 1 and 2, and Supplementary Information), please visit http://dx.doi.org/10.1017/S1431927613000342.

Segmentation of Dopant Segregation

To extract quantitative information about the different types of segregation—to grain boundaries, to precipitates, and to voids—we must first segment the reconstructed volumes into selenium rich and nonselenium rich regions. For the segmentation procedure, we used preprocessing steps for the normalization and filtering of the volumes combined

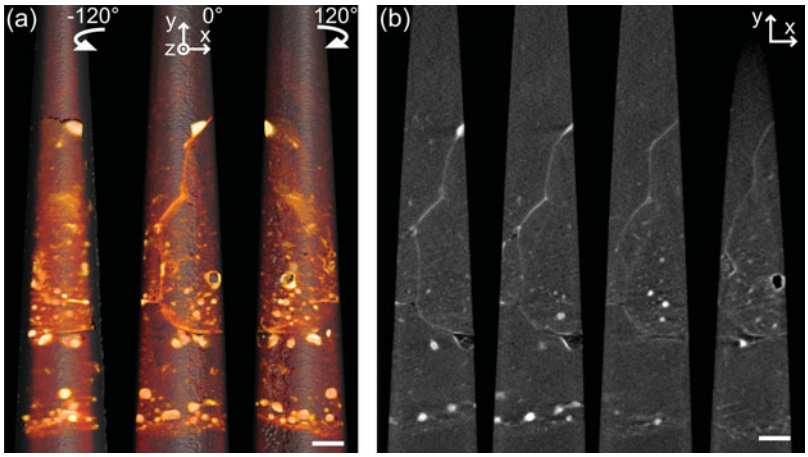

Figure 6. 3D reconstruction of the sample annealed at 950°C for 30 min: (**a**) Volume-rendered view from different viewing angles. Brighter regions correspond to higher selenium concentration. (**b**) Slices through the reconstructed volume at different locations along the *z*-direction. Strong signs of segregation to precipitates and grain boundaries as well as to voids are visible. The diffuse contrast is reduced compared to the nonannealed sample. Scale bars = 100 nm. An animation showing all slices can be found as Supplementary Movie 2.

with a gradient watershed segmentation algorithm (Adams & Bischof, 1994; Fernandez, 2012). An evaluation of the proposed segmentation method and on effects of missing wedge artifacts for a simulated object can be found as Supplementary Material.

Other methods—such as discrete tomography (Bals et al., 2007; Batenburg et al., 2009) or total-variation (TV) minimization based reconstruction (Saghi et al., 2011; Goris et al., 2012*b*)—use prior knowledge about discreteness of the material phases in the sample to combine reconstruction and segmentation or to obtain a filtered volume in the case of discrete tomography and TV-minimization based reconstruction, respectively. In our case, we decouple reconstruction and segmentation, as no discrete interfaces of selenium-rich material throughout the sample are expected due to the nature of the dopant incorporation and segregation. In addition, in the segmentation process we focus on regions with bright contrast relative to their close surroundings, rather than defining a specific dopant concentration threshold of interest.

To more clearly illustrate this segmentation process designed for quantifying dopant segregation in a disordered environment and from an initially inhomogeneous distribution, Figure 7 shows slices through the reconstructed volume before and after each step of the segmentation routine. The intensity profile, extracted along the indicated intersection, illustrates the evolution in signal noise from this segmentation process. Our segmentation routine consists of the following steps:

- *Normalization along height [Fig. 7 (1) → (2)]:* Starting from the original reconstructed volumes, in the first step we compensate for changes in overall dopant concentration with height of the sample (*y*-direction), visible in particular for the nonannealed sample. With this normalization, we put the gray level of regions between precipitates to approximately constant values for the whole sample, thus compensating for the increasing concentration of selenium in solid solution toward the base of the peaks. This normalization allows emphasis on the regions that have a high dopant concentration relative to their close surroundings. For this purpose we calculate the mean intensity at each height in the sample and do a linear interpolation along the height. Then we normalize all values at a given height with the value extracted from the interpolation. This provides a volume with relatively

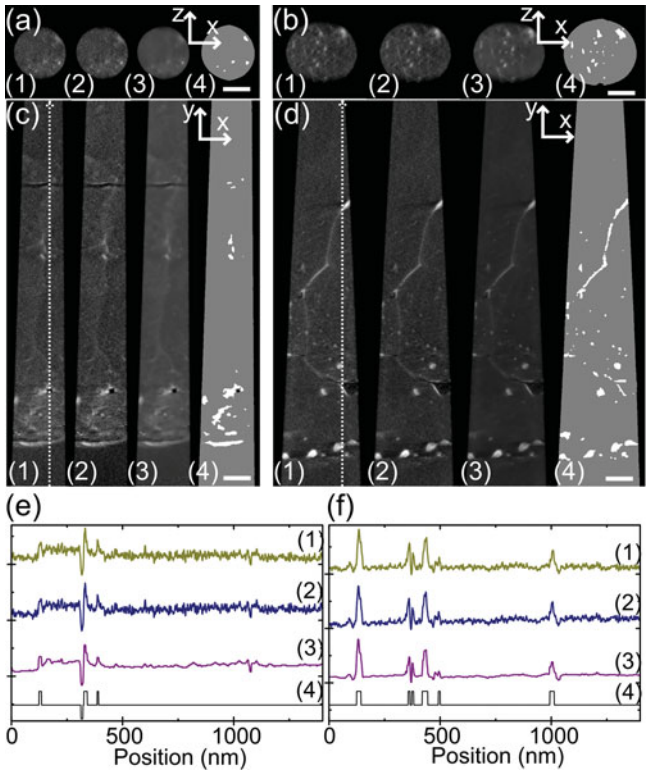

Figure 7. Steps of the data segmentation process: (**a**) slices through the nonannealed sample along an *xz*-plane and (**b**) slices through the 950°C annealed sample along an *xz*-plane. The slices along the *xz*-planes also illustrate the effects of missing wedge artifacts. (**c**) Slices through the nonannealed sample along an *xy*-plane, (**d**) slices through the 950°C annealed sample along an *xy*-plane, (**e**) intensity profiles along *z*-direction at the position indicated by a dashed arrow in panel **c**, and (**f**) intensity profiles along *z*-direction at the position indicated by a dashed arrow in panel **d**. The segmentation process starts from the original volume (1), to a volume normalized along the height (2), to a volume filtered using an anisotropic diffusion filter (3), and finishes with the final segmented volume (4). Scale bars = 100 nm.

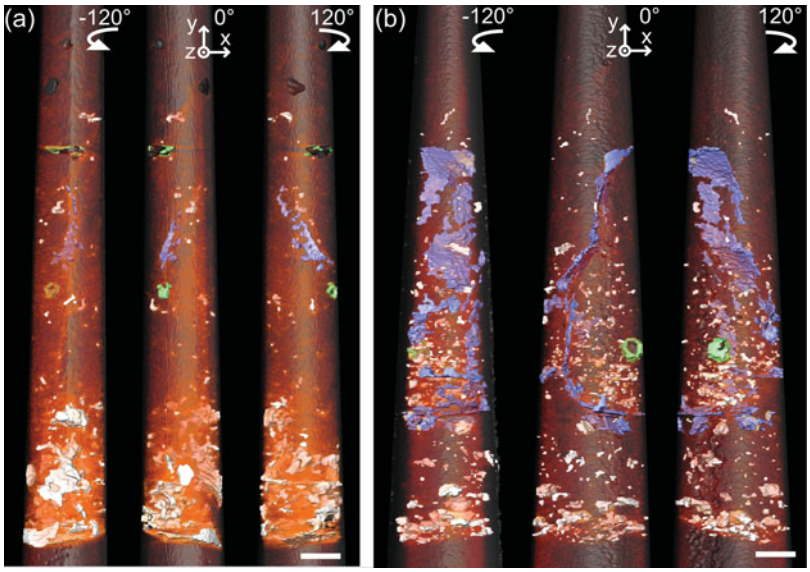

Figure 8. Surface rendered views of segmented reconstructions overlaid with volume-rendered views for (**a**) nonannealed sample and (**b**) 950°C annealed sample seen from different viewing angles. The volumes show segregation to precipitates (white), to grain boundaries (blue), and to voids (green). Scale bars = 100 nm.

constant gray values in the region between the precipitates, which facilitates the following segmentation step.

- *Filtering [Fig. 7 (2) → (3)]:* After the normalization we apply an anisotropic diffusion filter (Perona & Malik, 1990) to the volume to reduce noise in the reconstruction. A 3D version of the filter proposed by Perona and Malik, implemented in C, was used for filtering. Anisotropic diffusion filtering has been shown to be an efficient tool for edge-preserving denoising of electron tomograms and is frequently used in biological applications (Frangakis & Hegerl, 2001; Fernandez & Sam, 2005; Narasimha et al., 2008). The effects of filtering can be seen in the profiles, as the strong signals from segregated regions are conserved, while regions in between are smoothed.
- *Segmentation [Fig. 7 (3) → (4)]:* For the actual segmentation we use a gradient watershed algorithm (Adams & Bischof, 1994). Related segmentation methods have been proven efficient for segmentation of electron tomograms of biological samples (Volkmann, 2002; Salvi et al., 2008; Fernández-Busnadiego et al., 2010). Segmentation is done using the Avizo® software. First, regions with a large gradient are masked in such a way that transition regions between the materials are defined and will be subject to automated segmentation. In the remaining volume, seed regions, which belong to a specific material, are defined based on absolute threshold values. These two steps necessitate input from the user to define the threshold for the gradient mask and to set the ranges for the threshold value. For the actual segmentation a watershed transform is applied to the gradient volume to allocate masked voxels and voxels lying between the thresholded intervals. The watershed transform sets the boundary between seed regions of different materials to the position of the highest gradient.

This process produces volumes in which segregates are discretely separated from other regions of silicon. We can identify segregation at grain boundaries, segregation in the form of precipitates, and segregation toward the exposed surfaces of voids. Figure 8 shows the results of the segmentation, using different colors for the three types of segregation. This segmentation allows us to move forward quantifying the effect of annealing on segregation of selenium from the supersaturated silicon.

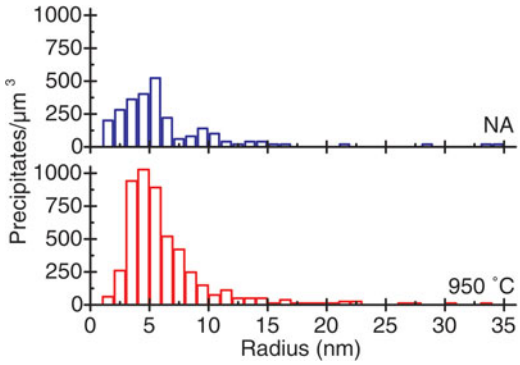

Figure 9. Size distribution of precipitates before annealing (blue) and after a 950°C anneal for 30 min (red). The number of precipitates has been normalized by the overall volume measured to take into account the slightly different volumes characterized. The size distribution shows a significant increase in the density of precipitates with annealing.

Quantification of Dopant Segregation

Qualitative inspection of the volumes reconstructed before and after annealing reveals results consistent with the previous cross-sectional TEM investigations: differences can be observed in the number of precipitates, which increases significantly with annealing, and also in the contrast observed in the region between the segregates, which is significantly lower in the annealed sample. Motivated by these qualitative observations, we extract quantitative information about the size and density of precipitates and the change in selenium concentration in solid solution in the regions between precipitates.

- *Precipitate size and density:* For this measure we focus only on segregation to precipitates to get information

about their size and distribution, excluding segregation to grain boundaries and voids. For this purpose the volume of each precipitate is extracted using the 3D object counter plugin for ImageJ. The volume of each precipitate is transformed to an equivalent radius of a sphere with the corresponding volume. The number of precipitates is converted to a precipitate density distribution by normalizing the number of precipitates with respect to the total volume of the investigated sample. The resulting size distribution for both samples is shown in Figure 9. We observe a significant increase in the density of precipitates with annealing, in particular a large number of relatively small precipitates is present after annealing, with 67% of the precipitates having a radius $r = 5\ (\pm 2)$ nm. A drawback of this technique is that the sample volume is too small to get a sufficient amount of data to quantify the evolution of larger precipitates ($r > 10$ nm) with annealing.

- *Background dopant concentration:* The segmented volumes can also be used to extract information about the dopant concentration in the regions between segregates. This process is shown in Figure 10a. We create a mask of all voxels that are attributed to silicon but do not belong to any type of segregation. Then a morphological erosion operator in 3D is applied several times on this mask using the ImageJ plugin 3D Toolkit. This step removes voxels close to the boundary of the volume and close to segregates. This mask is overlaid with the original reconstructed volume. The masked volume then contains only regions that are between the segregates and therefore provides information about changes in the amount of selenium in this area. Figure 10b shows the average intensity of each slice of the masked volume along the height for the two samples. The comparison of this background intensity shows clearly the changes of dopant concentration with height in both samples as well as the reduction of dopant concentration with annealing in the regions between segregates.

We note, however, that the values extracted from quantification of electron tomography reflect only the behavior in a small volume, and this makes correlation of the observed trends on the nanoscale with bulk properties a challenge. However, complementary experiments, using a more global probe such as EXAFS spectroscopy, can be used to confirm the trends on a larger scale (Newman et al., 2009). Finally, very small precipitates (radius $<$ 1–2 nm) cannot be detected due to the spatial resolution limit, which can be estimated to approximately 3 nm for the used number of projections (Midgley & Weyland, 2003). Therefore, segregation on atomic length scales is below the detection limits of electron tomography.

Results and Discussion

Our initial HAADF-STEM investigations provide direct evidence of selenium segregation with annealing, which supports previous hypotheses that diffusion-limited segregation is responsible for the optical deactivation of selenium with annealing (Tull et al., 2009). The HAADF-STEM results highlight the potential significance of the nucleation and growth of a Se-rich phase during the optical deactivation process.

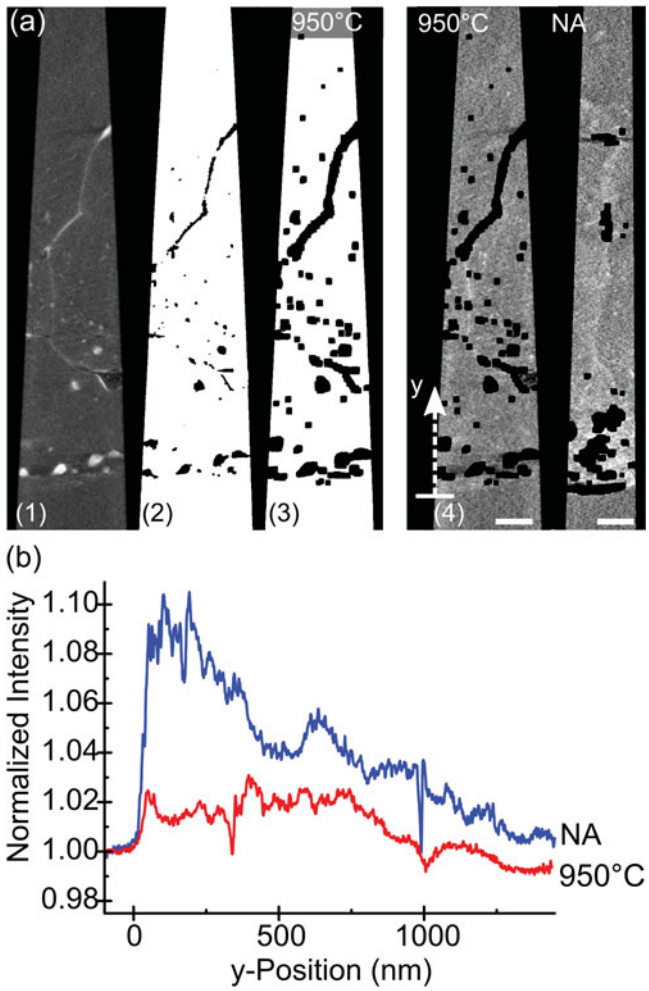

Figure 10. (**a**) Quantification of dopant concentration in the region between segregates: (1) slice through the original volume, (2) slice through the mask containing background voxels, (3) slice through the mask after morphological erosion for the 950°C annealed sample, and (4) slices through the masked volume for both samples (brightness/contrast settings are adapted compared to previous images): these voxels are used to calculate the normalized background intensity. (**b**) Normalized background intensity for the nonannealed sample (blue) and for the 950°C annealed sample (red) as a function of height. The distance is given from the interface to the undoped region toward the top of the samples as indicated in panel **a** (4). The extracted background intensity shows changes of dopant concentration with height for both samples and a reduction of dopant concentration in the region between segregates with annealing. Scale bars = 100 nm.

Characterization of a nonannealed sample using both cross-sectional TEM investigations and electron tomography allows for the identification of a representative microstructure and dopant distribution. Using *Z*-contrast to monitor the selenium distribution, we find an inhomogeneous distribution of dopants even before annealing. We observe an increasing concentration of dopants toward the

base of the peak, until it reaches a relatively sharp interface with the unmodified silicon wafer underneath. A diffuse bright contrast is visible in the nonannealed sample, which indicates a solid solution of selenium in silicon (Figs. 3, 5). Se-rich precipitates can also be observed, in particular at the base of the peak (Fig. 8a). The initial segregation of selenium from the supersaturated solid solution is likely a consequence of the annealing that occurs during scanning of the pulsed laser beam over the surface (Smith et al., 2012).

After annealing for 30 min at 950°C, we observe more localized Se-rich regions, providing direct evidence of dopant segregation in both cross sectional (Fig. 4) as well as in tomography investigations (Fig. 6). Electron tomography reveals a large number of small precipitates (Fig. 8b) and allows for quantification of their density and size distribution. Tomography shows that the size and number of these precipitates decreases toward the top of the peak, where there was less selenium observed in solid solution in the nonannealed sample. Quantification of the size distribution and density of precipitates (Fig. 9) confirms the formation of a large number of precipitates with annealing. The precipitates form throughout the investigate volume and in a larger number in the region with a higher initial supersaturation (bottom of the peak).

Grain boundary segregation is observable by comparing the *Z*-contrast of a grain boundary in the nonannealed and 950°C annealed samples. Close investigation of grain boundaries in the cross-sectional nonannealed sample (Figs. 3d, 3e) showed no signs of segregation, while in the annealed sample a few-nm-thick Se-rich layer is visible at the grain boundary (Figs. 4d, 4e). Similar trends are observed in the tomography reconstructions. Though here the reconstruction of the nonannealed sample (Figs. 5, 8a) shows weak signs of segregation at a grain boundary, in the annealed sample (Figs. 6, 8b) segregation is significantly enhanced and a Se-rich layer is clearly visible at the grain boundary.

It is understood that the sub-band gap absorptance shown in Figure 1b arises due to high concentrations of chalcogens being incorporated into silicon as a metastable, supersaturated, solid solution (Sheehy et al., 2007). Therefore, it is the decrease in supersaturation of silicon that is directly related to the optical properties of the material. The quantification of the contrast in the silicon matrix (Fig. 10) shows a significant reduction with annealing, which corresponds to a lower amount of selenium supersaturation in the annealed sample as compared to the nonannealed sample. In particular in the most highly doped regions, toward the base of the cylinder, this contrast arising due to selenium supersaturation is several times higher in the nonannealed sample than in the annealed sample.

The studies performed here provide elemental confirmation of chalcogen diffusion and segregation occurring as sub-band gap optical absorptance decreases. Previously this theory enjoyed only circumstantial support (Tull et al., 2009). We observe the segregation of dopants toward precipitates, grain boundaries, and voids, while at the same time the concentration of dopants in the material between the segregates decreases. The observations support the theory of diffusion-limited segregation being a major driving force behind the reduced sub-band gap absorptance with annealing, specifically during relatively long annealing at high temperatures.

Combined with volume segmentation methods, electron tomography can be used for quantitative investigation of a large number of small precipitates and also to monitor changes in contrast of the surrounding matrix. With a proper calibration sample, it may be possible to use the contrast observed in HAADF-STEM tomography to quantify the composition of the segregating phase and the surrounding supersaturated matrix.

Conclusions

In this work we have provided direct experimental evidence of selenium segregation with annealing of fs laser-doped silicon, which is likely a critical mechanism behind the reduced IR absorptance of silicon hyperdoped with chalcogens with annealing. Through 3D investigations using electron tomography based on HAADF-STEM, we observed segregation to precipitates, to grain boundaries, and to voids. Quantification of the distribution of dopant-rich regions can provide insight into the kinetics of dopant segregation, and eventually such methods could be also extended toward absolute quantification of dopant concentration.

Acknowledgments

This work was supported by the MIT-France MISTI program and by the French Recherche Technologie de Base (RTB) program. The authors acknowledge access to the nanocharacterization platform (PFNC) at Minatec Campus in Grenoble. Investigations were also supported by the Chesonis Family Foundation and by Oak Ridge National Laboratory's Shared Research Equipment (ShaRE) User Facility Program (JCI), which is sponsored by the Office of Basic Energy Sciences, the U.S. Department of Energy. M.W. acknowledges support from the National Science Foundation Graduate Research Fellowship Program.

References

Adams, R. & Bischof, L. (1994). Seeded region growing. *IEEE Trans Pattern Anal Mach Intell* **16**, 641–647.

Bals, S., Batenburg, K.J., Verbeeck, J., Sijbers, J. & Van Tendeloo, G. (2007). Quantitative three-dimensional reconstruction of catalyst particles for bamboo-like carbon nanotubes. *Nano Lett* **7**, 3669–3674.

Bals, S., Casavola, M., van Huis, M.A., Van Aert, S., Batenburg, K.J., Van Tendeloo, G. & Vanmaekelbergh, D.L. (2010). Three-dimensional atomic imaging of colloidal core-shell nanocrystals. *Nano Lett* **11**, 3420–3424.

Batenburg, K.J., Bals, S., Sijbers, J., Kübel, C., Midgley, P.A., Hernandez, J.C., Kaiser, U., Encina, E.R., Coronado, E.A. & Van Tendeloo, G. (2009). 3D imaging of nanomaterials by discrete tomography. *Ultramicroscopy* **109**, 730–740.

Carey, J.E., Crouch, C.H., Shen, M. & Mazur, E. (2005). Visible and near-infrared responsivity of femtosecond-laser microstructured silicon photodiodes. *Opt Lett* **30**, 1773–1775.

Duguay, S., Colin, A., Mathiot, D., Morin, P. & Blavette, D. (2010). Atomic-scale redistribution of dopants in polycrystalline silicon layers. *J Appl Phys* **108**, 034911.

Fernandez, J.-J. (2012). Computational methods for electron tomography. *Micron* **43**, 1010–1030.

Fernandez, J.J. & Sam, L. (2005). Anisotropic nonlinear filtering of cellular structures in cryoelectron tomography. *Comput Sci Eng* **7**, 54–61.

Fernández-Busnadiego, R., Zuber, B., Maurer, U.E., Cyrklaff, M., Baumeister, W. & Lučić, V. (2010). Quantitative analysis of the native presynaptic cytomatrix by cryoelectron tomography. *J Cell Biol* **188**, 145–156.

Frangakis, A.S. & Hegerl, R. (2001). Noise reduction in electron tomographic reconstructions using nonlinear anisotropic diffusion. *J Struct Biol* **135**, 239–250.

Gilbert, P. (1972). Iterative methods for the three-dimensional reconstruction of an object from projections. *J Theor Biol* **36**, 105–117.

Goris, B., Bals, S., Van den Broek, W., Carbó-Argibay, E., Gómez-Graña, S., Liz-Marzán, L.M. & Van Tendeloo, G. (2012*a*). Atomic-scale determination of surface facets in gold nanorods. *Nat Mater* **11**, 930–935.

Goris, B., Van den Broek, W., Batenburg, K.J., Heidari Mezerji, H. & Bals, S. (2012*b*). Electron tomography based on a total variation minimization reconstruction technique. *Ultramicroscopy* **113**, 120–130.

Hyun, J.K., Ercius, P. & Muller, D.A. (2008). Beam spreading and spatial resolution in thick organic specimens. *Ultramicroscopy* **109**, 1–7.

Jin, S., Jones, K.S., Law, M.E. & Camillo-Castillo, R. (2012). B segregation to grain boundaries and diffusion in polycrystalline Si with flash annealing. *J Appl Phys* **111**, 044508.

Kaneko, K., Inoke, K., Sato, K., Kitawaki, K., Higashida, H., Arslan, I. & Midgley, P.A. (2008). TEM characterization of Ge precipitates in an Al-1.6 at% Ge alloy. *Ultramicroscopy* **108**, 210–220.

Kawase, N., Kato, M., Nishioka, H. & Jinnai, H. (2007). Transmission electron microtomography without the "missing wedge" for quantitative structural analysis. *Ultramicroscopy* **107**, 8–15.

Ke, X., Bals, S., Cott, D., Hantschel, T., Bender, H. & Van Tendeloo, G. (2010). Three-dimensional analysis of carbon nanotube networks in interconnects by electron tomography without missing wedge artifacts. *Microsc Microanal* **16**, 210–217.

Midgley, P.A. & Dunin-Borkowski, R.E. (2009). Electron tomography and holography in materials science. *Nat Mater* **8**, 271–280.

Midgley, P.A. & Weyland, M. (2003). 3D electron microscopy in the physical sciences: The development of Z-contrast and EFTEM tomography. *Ultramicroscopy* **96**, 413–431.

Narasimha, R., Aganj, I., Bennett, A.E., Borgnia, M.J., Zabransky, D., Sapiro, G., McLaughlin, S.W., Milne, J.L.S. & Subramaniam, S. (2008). Evaluation of denoising algorithms for biological electron tomography. *J Struct Biol* **164**, 7–17.

Newman, B.K., Sullivan, J.T., Winkler, M.T., Sher, M.J., Marcus, M.A., Fakra, S., Smith, M.J., Gradečak, S., Mazur, E. & Buonassisi, T. (2009). Illuminating the mechanism for subbandgap absorption in chalcogen doped silicon materials for PV applications. In *24th European Photovoltaic Solar Energy Conference*, pp. 236–238.

Perona, P. & Malik, J. (1990). Scale-space and edge detection using anisotropic diffusion. *IEEE Trans Pattern Anal Mach Intell* **12**, 629–639.

Saghi, Z., Holland, D.J., Leary, R., Falqui, A., Bertoni, G., Sederman, A.J., Gladden, L.F. & Midgley, P.A. (2011). Three-dimensional morphology of iron oxide nanoparticles with reactive concave surfaces. A compressed sensing-electron tomography (CS-ET) approach. *Nano Lett* **11**, 4666–4673.

Salvi, E., Cantele, F., Zampighi, L., Fain, N., Pigino, G., Zampighi, G. & Lanzavecchia, S. (2008). JUST (Java User Segmentation Tool) for semi-automatic segmentation of tomographic maps. *J Struct Biol* **161**, 287–297.

Schierning, G., Theissmann, R., Stein, N., Petermann, N., Becker, A., Engenhorst, M., Kessler, V., Geller, M., Beckel, A., Wiggers, H. & Schmechel, R. (2011). Role of oxygen on microstructure and thermoelectric properties of silicon nanocomposites. *J Appl Phys* **110**, 113515.

Scott, M.C., Chen, C.-C., Mecklenburg, M., Zhu, C., Xu, R., Ercius, P., Dahmen, U., Regan, B.C. & Miao, J. (2012). Electron tomography at 2.4-angstrom resolution. *Nature* **483**, 444–447.

Sheehy, M.A., Tull, B.R., Friend, C.M. & Mazur, E. (2007). Chalcogen doping of silicon via intense femtosecond-laser irradiation. *Mater Sci Eng B* **137**, 289–294.

Sher, M.J., Winkler, M.T. & Mazur, E. (2011). Pulsed-laser hyperdoping and surface texturing for photovoltaics. *MRS Bull* **36**, 439–445.

Smith, M., Winkler, M., Sher, M.-J., Lin, Y.-T., Mazur, E. & Gradečak, S. (2011*a*). The effects of a thin film dopant precursor on the structure and properties of femtosecond-laser irradiated silicon. *Appl Phys A* **105**, 795–800.

Smith, M.J., Lin, Y.-T., Sher, M.-J., Winkler, M.T., Mazur, E. & Gradečak, S. (2011*b*). Pressure-induced phase transformations during femtosecond-laser doping of silicon. *J Appl Phys* **110**, 053524.

Smith, M.J., Sher, M.-J., Franta, B., Lin, Y.-T., Mazur, E. & Gradečak, S. (2012). The origins of pressure-induced phase transformations during the surface texturing of silicon using femtosecond laser irradiation. *J Appl Phys* **112**, 083518.

Thompson, K., Booske, J.H., Larson, D.J. & Kelly, T.F. (2005). Three-dimensional atom mapping of dopants in Si nanostructures. *Appl Phys Lett* **87**, 052108.

Tull, B., Winkler, M. & Mazur, E. (2009). The role of diffusion in broadband infrared absorption in chalcogen-doped silicon. *Appl Phys A* **96**, 327–334.

Tull, B.R., Carey, J.E., Mazur, E., McDonald, J.P. & Yalisove, S.M. (2006). Silicon surface morphologies after femtosecond laser irradiation. *MRS Bull* **31**, 626–633.

Van Aert, S., Batenburg, K.J., Rossell, M.D., Erni, R. & Van Tendeloo, G. (2011). Three-dimensional atomic imaging of crystalline nanoparticles. *Nature* **470**, 374–377.

Van Aert, S., Verbeeck, J., Erni, R., Bals, S., Luysberg, M., Dyck, D.V. & Tendeloo, G.V. (2009). Quantitative atomic resolution mapping using high-angle annular dark field scanning transmission electron microscopy. *Ultramicroscopy* **109**, 1236–1244.

Van den Broek, W., Rosenauer, A., Goris, B., Martinez, G.T., Bals, S., Van Aert, S. & Van Dyck, D. (2012). Correction of non-linear thickness effects in HAADF STEM electron tomography. *Ultramicroscopy* **116**, 8–12.

Volkmann, N. (2002). A novel three-dimensional variant of the watershed transform for segmentation of electron density maps. *J Struct Biol* **138**, 123–129.

Vydyanath, H.R., Lorenzo, J.S. & Kroger, F.A. (1978). Defect pairing diffusion, and solubility studies in selenium-doped silicon. *J Appl Phys* **49**, 5928–5937.

Wu, C., Crouch, C.H., Zhao, L., Carey, J.E., Younkin, R., Levinson, J.A., Mazur, E., Farrell, R.M., Gothoskar, P. & Karger, A. (2001). Near-unity below-band-gap absorption by microstructured silicon. *Appl Phys Lett* **78**, 1850–1852.

Yaguchi, T., Konno, M., Kamino, T. & Watanabe, M. (2008). Observation of three-dimensional elemental distributions of a Si device using a 360°-tilt FIB and the cold field-emission STEM system. *Ultramicroscopy* **108**, 1603–1615.

Younkin, R., Carey, J.E., Mazur, E., Levinson, J.A. & Friend, C.M. (2003). Infrared absorption by conical silicon microstructures made in a variety of background gases using femtosecond-laser pulses. *J Appl Phys* **93**, 2626–2629.